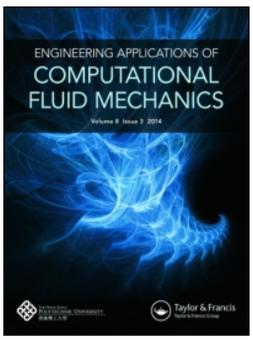

Taylor & Francis
Taylor & Francis Group

Engineering Applications of Computational Fluid Mechanics

ISSN: (Print) (Online) Journal homepage: https://www.tandfonline.com/loi/tcfm20

Development of CFD-based procedure for 3d gear pump analysis

Jernej Munih , Marko Hočevar , Klemen Petrič & Matevž Dular

To cite this article: Jernej Munih , Marko Hočevar , Klemen Petrič & Matevž Dular (2020) Development of CFD-based procedure for 3d gear pump analysis, Engineering Applications of Computational Fluid Mechanics, 14:1, 1023-1034, DOI: 10.1080/19942060.2020.1789506

To link to this article: https://doi.org/10.1080/19942060.2020.1789506

ENGINEERING APPLICATIONS OF COMPUTATIONAL FLUID MECHANICS
2020, VOL. 14, NO. 1, 1023–1034
https://doi.org/10.1080/19942060.2020.1789506

Taylor & Francis
Taylor & Francis Group

Development of CFD-based procedure for 3d gear pump analysis

Jernej Munih[a], Marko Hočevar[b], Klemen Petrič[a] and Matevž Dular[b]

[a]Kolektor Group d.o.o., Idrija, Slovenia; [b]Laboratory for Water and Turbine Machines, University of Ljubljana, Ljubljana, Slovenia

ABSTRACT

Tumbling Multi-Chamber (TMC) gear pump is a generally unknown type of hydraulic device, which features a unique three-dimensional shape of the gears. The main benefits of such design over the conventional gear pumps are self-adapting tightness of the pump parts, the possibility to mold the parts from a polymer material and high volumetric efficiency, considering the simplicity of the design. The specific working principle of TMC pumps requires a slightly different approach to the numeric modeling and analysis process compared to the conventional gear pump types (e.g. external gear and gerotor pumps). One of the main contributions of the work is the development of an analysis procedure, which allows studying flow and pressure conditions in the TMC pump. This includes the influence of the positioning of the pump parts on spatial and temporal variations in sealing regions and the influence of pressure field propagation in relation to the valve plate position.

ARTICLE HISTORY
Received 5 February 2020
Accepted 2 June 2020

KEYWORDS
Tumbling multi-chamber; gear pump; CFD; volumetric; experimental

1. Introduction

Positive displacement (PD) pumps often feature two-dimensional shapes for simple design and reliable operation. In last years, a novel type of PD pumps emerged, among them Tumbling Multi-Chamber (TMC) pump with the three-dimensional shape of the gears, which can be seen in Figure 1. In comparison with currently established gear pumps, it offers the following advantages: self-adapting tightness of the pump parts during the wear process, the possibility to mold the parts from a polymer material, compact design and high volumetric efficiency for a reasonable cost. The advantages enable use in many applications, for which current PD pumps are less suitable.

Between other PD pumps and TMC pumps, we see important differences that have an effect on the CFD modeling procedure for TMC pumps. Among them are the motion of pump runner, including its characteristic tumbling motion, and resulting spatial and continuous 3d variations of sealing regions. The CFD modeling procedure must therefore consider TMC pump-specific requirements.

Basic components of the pump, which is discussed in the following study, are the shaft, the stator with z-teeth, and the runner with $z+1$ teeth, all of which are shown in Figure 1. Motion sequence of the assembled parts is shown in Figure 2. View (a) shows the initial state of the pump parts, whereas (b–e) show the shaft angles of 60°, 120°, 240° and 300°, respectively.

The motion consists of the rotation of the shaft (3) and the tumbling motion of the runner (2). In the assembled position (see Figure 2), the runner is tilted for a constant pre-defined angle with respect to the rotation axis of the shaft.

Transfer of the torque from the shaft to the pump runner is performed via a slanted plane, which also works as a valve plate (see Figure 2). Functions of the valve plate (4) are to separate low and high-pressure regions of the pump and to alternately open and close the channels between the flat sliding surface and the three-dimensional toothed surface of the runner.

Tumbling motion of the runner induces suction and displacement of the fluid into and out of the working chambers. Figure 3 shows the fluid volume, which is enclosed by the surfaces of the stator and the runner. Directions of the inlet flows are represented with dashed lines, and the directions of the outlet flows are represented with the solid lines.

The basic concepts of the TMC pump technology are not unknown, as they are comprehensively described in the documents by Wildhaber (1966, 1974), Arnold (1993) and in the related documents. In addition to these documents, we have found no publicly available scientific reports about TMC pumps. There is, however, extensive amount of scientific research performed on other PD pumps.

The pump under investigation belongs to the group of positive displacement (PD) pumps, which were

CONTACT Jernej Munih jernej.munih@kolektor.com, jernej.m@siol.net

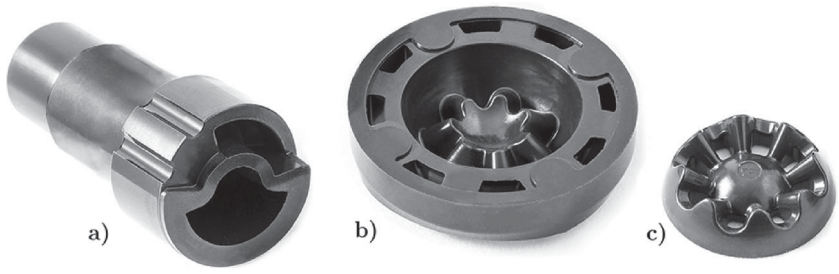

Figure 1. (a) Pump shaft, (b) stator, and (c) the runner.

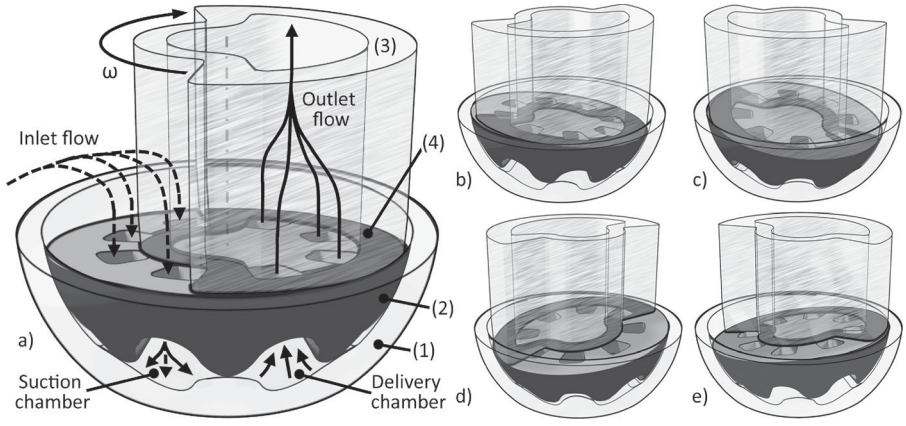

Figure 2. Presentation of different positions of the shaft (3) and the runner (2) in relation to the stator (1). View (a) shows shaft rotation and flow directions in the initial position. Following views show shaft rotation angles of (b) 60°, (c) 120°, (d) 240°, and (e) 300°.

researched by numerous authors in the past years (Chao et al., 2019; Iannetti et al., 2016). One of the most extensive papers on this topic is the review by Gamez-Montero et al. (2019), who listed 166 research items that refer to the gerotor technology. One of the facts presented in the article is that 54% of existing items were published between the years 2014 and 2018. This shows that the topic is highly relevant.

Various studies on PD machines cover manufacturing processes (Chen et al., 2018), surface engineering (Strmčnik et al., 2019), design modifications (Kim et al., 2006), optimization techniques (Robison & Vacca, 2018) and visualization methods (Antoniak & Stryczek, 2018). Papers featuring analytic and numerical approaches for analysis of gerotor, internal gear (crescent) and external gear pumps were reviewed by Rundo (2017). The author classifies simulation models in 0d (lumped-parameter), 1d or 2d–3d (CFD).

Lumped parameter (LP) model of a pump comprising spur and helical gear pump stages was investigated by Battarra et al. (2015). Pellegri et al. (2016) used LP model to conduct an analysis of a gerotor pump. Spille-Kohoff

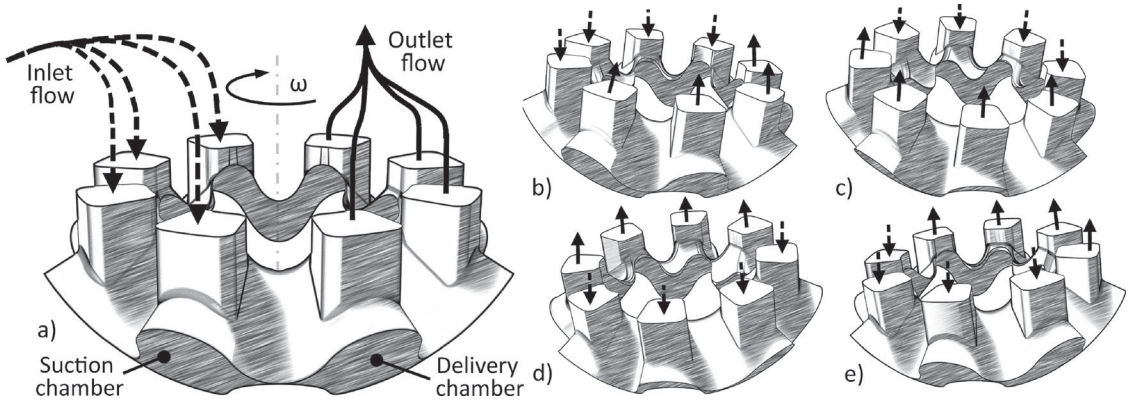

Figure 3. A fluid volume between the surfaces of the stator and the runner at different rotation angles of the shaft: (a) initial position, (b) 60°, (c) 120°, (c) 240°, and (d) 300°.

et al. (2017) stated that the main challenges in the case of performing 3d CFD simulations are mesh deformations during the rotation of the pump shaft, sliding between mesh regions and adequate resolution of the mesh inside of the thin gaps.

The review of prior investigations allows us to classify 3d simulation methods for rotary PD machines in the following groups:

(a) Structured or unstructured adaptive meshing (remeshing)
(b) Immersed Solid Method (ISM),
(c) Deformation of structured hexahedral grids,
(d) Chimera grid (also known as Overset grid) approach, and
(e) Smoothed particle hydrodynamics (SPH) approach.

An unstructured adaptive grid approach was used by Zhang et al. (2006) to analyze the flow and pressure ripple of a gerotor oil pump. Gerotor pump was also simulated and experimentally analyzed by Natchimuthu et al. (2010), who used a 2.5d meshing strategy. For each time step, new triangular mesh was generated first in 2d and then extruded into space. Liu et al. (2019) used the 2.5d mesh in combination with user-defined functions to simulate a crescent pump. Castilla et al. (2015) used open-source code and mesh replacement method to simulate rotary PD pump.

ISM method allows the simulation of the motion of solid objects inside of the fluid region without the need for mesh deformation or remeshing. Usage of the mentioned method for modeling of external gear pump was featured in the work by Yoon et al. (2017).

A prevailing part of numerical researches was done with the usage of algorithms, which deform structured hexahedral grids in each step of the simulation. For this purpose, different approaches were used. Kovacevic et al. (2003) generated an O-type grid around the geometry of the screw machine with the usage of 2d transfinite interpolation. Voorde et al. (2004) constructed the grids with a different approach, they used the solution of the Laplace equation to define an appropriate distribution of the nodes of the block-structured grid.

There were numerous studies performed using commercial codes purposely made for automated structured grid generation. Cavitation in gear pumps was researched by Spille-Kohoff and Hesse (2016) and Frosina et al. (2017). Zhao et al. (2018) compared LP and 3d CFD approach for the analysis of helical external gear pump with continuous-contact gear profile.

Altare and Rundo (2016) studied design parameters, which affect the filling in a gerotor pump and Hsieh (2012) analyzed the effects of various span angle designs. Gerotor pump was also a topic of the research by Castilla et al. (2017), who avoided the remeshing process with the combination of deforming mesh method and OpenFOAM solver.

Fundamentals of the Chimera grid approach were described by Steger et al. (1983) and Benek et al. (1986). The basic attribute of the method is the usage of multiple grids, which are described as a major grid and minor grids. The advantage of the usage of multiple grids is the simplification of the grid generation, as each grid can be generated independently. Ziviani et al. (2016) conducted a comparison between remeshing and Chimera grid methods in the case of scroll expander device. Nevertheless, there were no publications found that it would describe simulations of PD pumps using this CFD method.

SPH techniques are rarely used for numerical modeling of PD machines, as the work by Prakash et al. (2003) is the only one which covers this field. The authors of the mentioned study analyzed the shear stress field in the lobe pump while varying the gap size between the lobes and pump housing.

The objective of the following work was to develop a methodology of TMC pump analysis. The presented methodology could in the future be used as a basis for further research on the field of TMC pumps. For this, we reviewed options for TMC pump CFD modeling and developed the numerical model of the TMC pump with the usage of automatic grid generation method. By doing so, we explained how the theoretical positioning of the pump parts affects spatial and temporal variations in sealing regions and how this influences some of the hydraulic phenomena inside of the pump. Based on the results of CFD analysis, it was possible to explain, how the pressure fields propagate in relation to the valve plate position. The approach also allows an estimation of the flow through individual leakage paths.

Next section of the existent work reveals the numerical modeling process, which was used to simulate the TMC pump. The article continues with an overview of the experimental setup and testing conditions. The fourth section begins with mesh sensitivity analysis, continues with a display of flow-related data and concludes with revealing of pressure conditions together with the visualization of sealing regions.

2. Numerical modeling

2.1. Numerical strategy

A method based on Navier–Stokes equations and finite volume (FV) discretization was used to calculate the flow in the pump. During the transient simulation the control

volumes deform in time, therefore the modified integral conservation equations are used. The modifications follow from the application of the Leibnitz rule (Ansys cfx – solver theory guide: Release 14.0, 2011):

$$\frac{\mathrm{d}}{\mathrm{d}t}\int_{(t)}\varphi\,\mathrm{d}V=\int_{V}\frac{\partial\varphi}{\partial t}\,\mathrm{d}V+\int_{S}\varphi W_j\,\mathrm{d}n_j, \qquad (1)$$

where t is the time, φ is a general variable, V and s respectively denote volume and surface regions of the integration, W_j is the velocity of the control volume boundary and n_j represents differential Cartesian components of the outward normal surface vector.

For the modeling of the turbulence, Shear Stress Transport (SST) model (Menter, 1993; Menter et al., 2003) was used. The choice of the turbulence model allows achieving sufficient quality of the boundary layer, as well as the accuracy of free shear flow. Ansys CFX solver, which was used to conduct the calculations uses co-located grid arrangement and algorithm, proposed by Rhie and Chow (1983) for pressure-velocity coupling. Adopted solver uses an implicit method for the pressure–velocity coupling.

High-resolution advection scheme and second-order Backward Euler transient scheme were used. First-order upwind scheme was chosen for the modeling of turbulence.

2.2. Meshing process

The model of TMC pump with theoretical displacement $q_{theor} = 780\,\mathrm{mm}^3$/revolution was used as an input for the simulation. Initial CAD geometry of the fluid volume inside the pump was split into the regions, which are shown in Figure 4.

One of the main challenges when performing CFD analysis of PD pumps is the modeling of deforming volume between the working surfaces. Based on comprehensive study, which is briefly described in the introductory section of the existent article, usage of deforming structured grids was recognized as a suitable method for the modeling of the TMC pump.

Deforming mesh between 3d surfaces of pump stator and pump runner was generated using TwinMesh software, which allows to automatically generate structured hexahedral meshes. Mesh data was generated in advance and then imported to CFX on the beginning of each step with using of Junction Box Routine.

Time steps of $4.8\cdot10^{-5}$ s, $2.8\cdot10^{-5}$ s, $2.0\cdot10^{-5}$ s were used for the shaft rotation speeds of 3000 rpm, 5000 rpm and 7000 rpm, respectively. Deforming mesh in a 2d perspective is shown in Figure 5, while Figure 6 displays the mesh in 3d view together with the meshes, which represent the gaps between the spherical surfaces.

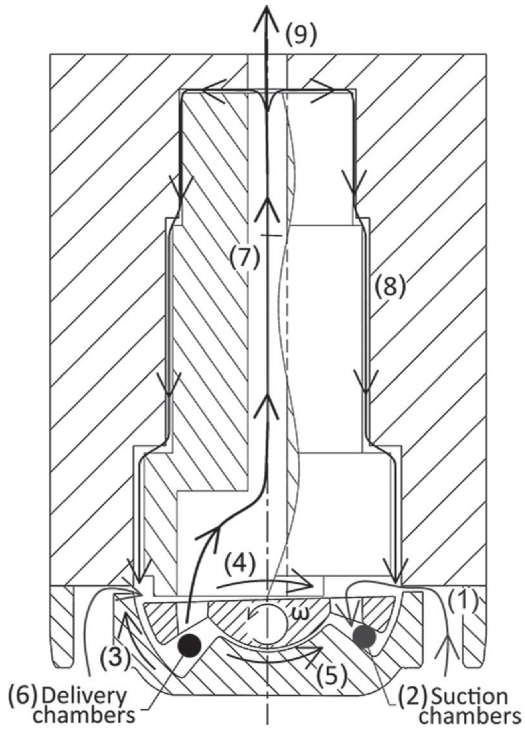

Figure 4. Regions and flow directions in the pump: (1) inlet channel, (2, 6) suction and delivery chambers, (3, 5) gaps between the spheres, (4) valve plate gap, (7) channel in the shaft, (8) journal bearings, and (9) outlet.

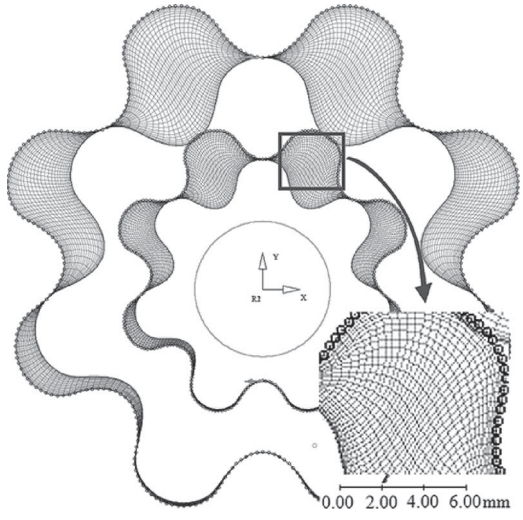

Figure 5. Deforming mesh in 2d perspective.

Two numerical models, which differ in complexity, were prepared. First, a simplified model was used for mesh sensitivity analysis. In this case, the fluid region consisted of the following regions (see Figure 4): inlet channel (1), the volume between 3d surfaces (2, 6) and outlet channel (7). Meshes, which represent thin gaps were excluded from the first model. Excluded regions were (see Figure 4): gaps between the spheres (3, 5), valve

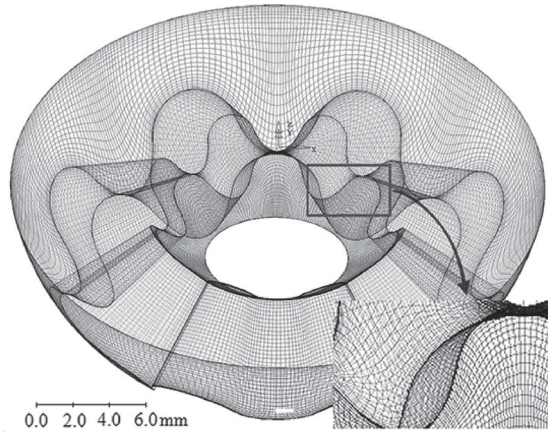

Figure 6. Mesh between pump stator and runner in 3d perspective.

plate gap (4) and the volume in journal bearings (9). The mesh, which represents the model used for the mesh sensitivity analysis, is shown in Figure 7.

Meshes used for mesh sensitivity analysis differ in the number of the elements of the deforming mesh. Variations were performed with changing the parameters in Twinmesh. Resulting meshes consisted of $1.3 \cdot 10^6$, $2.2 \cdot 10^6$ and $2.8 \cdot 10^6$ elements.

In the next step, the complete pump model was built. For this purpose, additional fluid regions were included (see Figure 4): gaps between the spheres (3, 5), valve plate gap (4) and the gap between journal bearings surfaces (8). Addition of the thin gaps allowed to achieve the complete representation of the fluid domain inside of the analyzed pump. Figure 8 shows the projection of complete mesh on the surface of the pump shaft.

Table 1 shows the number of the elements, and types of the elements, which were used for meshing of different regions. For major part of the mesh, hexahedral elements were used. In some regions, it was necessary to apply tetrahedron, pyramid, and wedge element types.

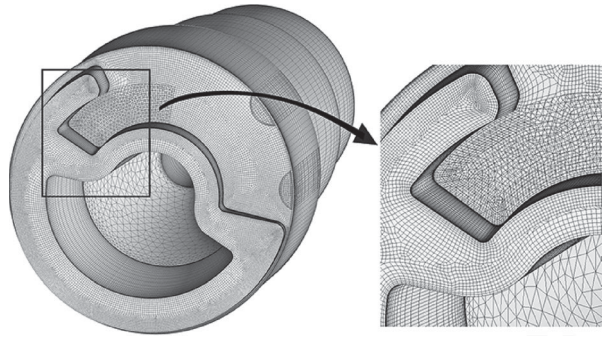

Figure 8. Imprint of the full mesh on the pump shaft surface.

Table 1. Mesh data by fluid regions, which were used for the full model of the pump.

Mesh region	Elements	Elements type
Inlet channel	$3.0 \cdot 10^5$	Hex
Deforming mesh	$1.7 \cdot 10^6$	Hex
Gaps between spheres	$2.1 \cdot 10^5$	Hex, Wed
Channels in the runner	$4.5 \cdot 10^5$	Hex, Wed
Out. channel, bearings	$2.3 \cdot 10^6$	Hex, Wed, Tet, Pyr
Global	$4.9 \cdot 10^6$	

Deforming mesh parameters for the complete model were chosen on the basis of results, which were obtained from the mesh sensitivity study.

Heights of the thin gaps inside of the pump were assumed on the basis of theoretical pump parts geometry, theoretical two-axis motion of the pump runner and ideally concentric position of the shaft.

Figure 9 shows a theoretical clearance between the stator and the runner. Thin dark regions on the 3d surface represent a sealing lines between separate working chambers. The theoretical clearance in the vicinity of the valve plate is shown in Figure 10. Both Figures 9 and 10 show the position of the parts in the first time step of the analysis.

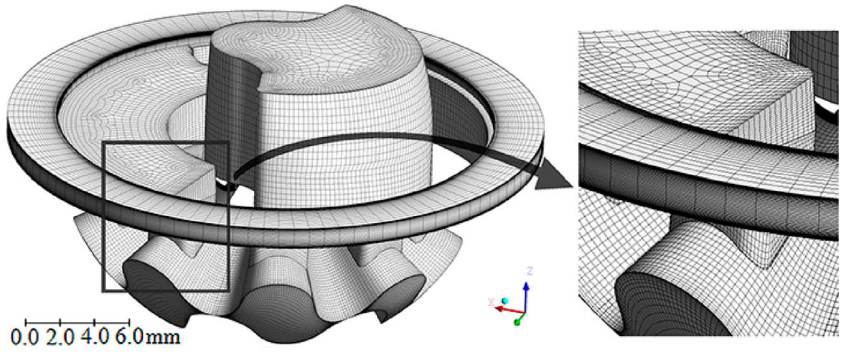

Figure 7. Simplified mesh, which was used for the mesh sensitivity analysis.

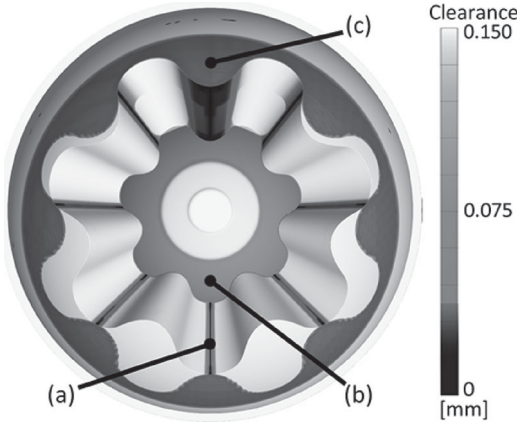

Figure 9. Example of theoretical clearance between pump stator and runner. Regions: (a) gears meshing region, (b) inner sliding sphere, and (c) outer sliding sphere.

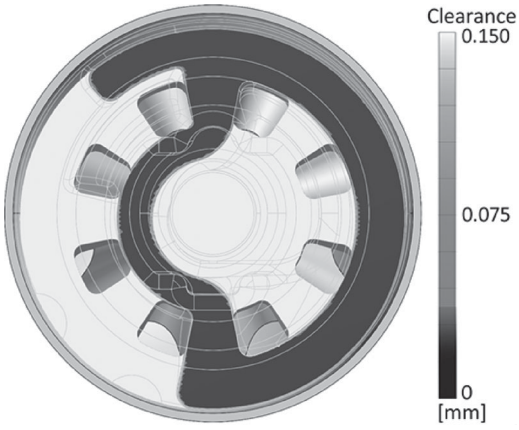

Figure 10. Example of theoretical clearance between pump runner and the shaft.

2.3. Boundary conditions

Nine different operating points (OPs) were simulated. The first varying-parameter was static pressure difference between the inlet and the outlet. Following pressure differences were used: 100 kPa, 500 kPa, and 1050 kPa. The second parameter was the rotation speed of the shaft, which took the values of 3000, 5000, and 7000 revolutions per minute (rpm).

Water at 25°C was used as a medium. Given liquid has a dynamic viscosity of $8.9 \cdot 10^{-4}$ Pa s and a density of 997 kg/m^3. No slip conditions were applied to the walls of the fluid regions.

3. Experimental

The experimental part was conducted on a test bench, which is schematically presented in Figure 11. Pump (3) was positioned at a height of 0.4 m above the water level. The first pressure sensor (2) (WIKA A-10, range

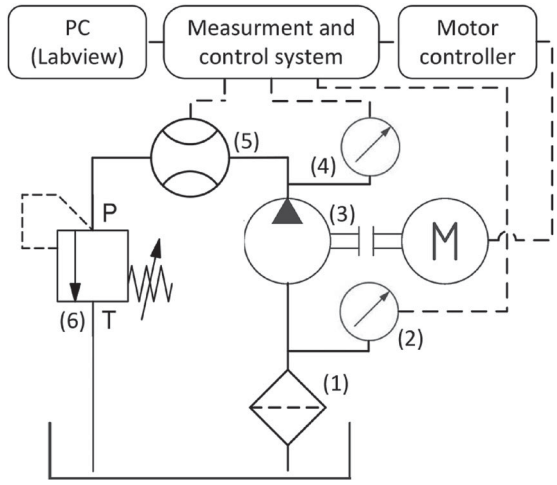

Figure 11. Scheme of the test bench. Hydraulic part consists of: (1) filter, pressure sensor on the suction side, (2) pump with integrated electric motor, (3) pressure sensor on the delivery side, (4) flow meter, and (5) pressure regulating valve.

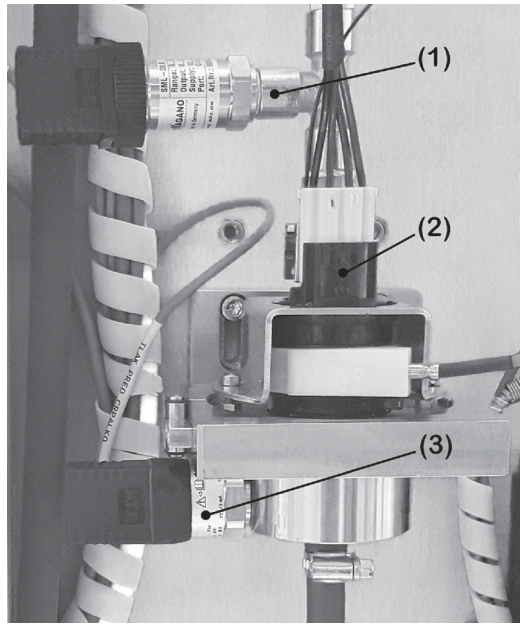

Figure 12. Pump mounting on the test bench: (1) pressure sensor on the delivery side, (2) TMC pump, and (3) pressure sensor on the suction side.

−1–0 bar) was mounted near the inlet of the pump and the second sensor (4) (WIKA A-10, range 0–16 bar) was positioned between the pump and a pressure regulating valve (6), as shown in Figure 12. Coriolis mass flow meter (5) (Micro Motion F025S) was positioned after the pressure valve.

The pump is driven by the motor, which is integrated into the pump assembly and thus forms a simple and compact design of the electronic pump. Such design was described by Kunath et al. (2016).

Measurements were obtained in 34 operating points. Pressure differences during the measuring were set to the values between 100 kPa and 1000 kPa. Range of the shaft speed was between 1100 and 7400 rpm. 60 measurements were acquired for each operating point with the sample rate of 2 Hz. Values were averaged during data processing.

Volumetric efficiency η_{vol} was calculated in the same manner from numeric and experimental data. Results are straightforwardly obtained from measured or simulated volumetric flow rate Q, theoretical displacement q_{theor}, and shaft speed n:

$$\eta_{vol} = \frac{Q}{q_{theor} \cdot n}. \tag{2}$$

4. Results and discussion

4.1. Mesh sensitivity analysis

Sensitivity analysis was performed at pressure difference 1000 kPa and shaft speed 3000 rpm. Figure 13 shows time-dependent volumetric efficiencies for different mesh densities. The shape of the curve, which represents the model with $1.3 \cdot 10^6$ elements, is less smooth compared with the other two volumetric efficiency curves. It is also clearly seen that in the case of meshing with $1.3 \cdot 10^6$ elements, the values of volumetric efficiency are generally lower than in case more elements were used.

Averaged values of volumetric efficiency in relation to the number of elements are shown in Figure 14. On the basis of sensitivity analysis, it was assumed that simplified model of the TMC pump can be sufficiently represented by $2.3 \cdot 10^6$ elements. At the analyzed operating point, the flow difference between the models with $2.3 \cdot 10^6$ and $2.8 \cdot 10^6$ elements is only 0.6 l/h, which corresponds to 0.4% difference in volumetric efficiency.

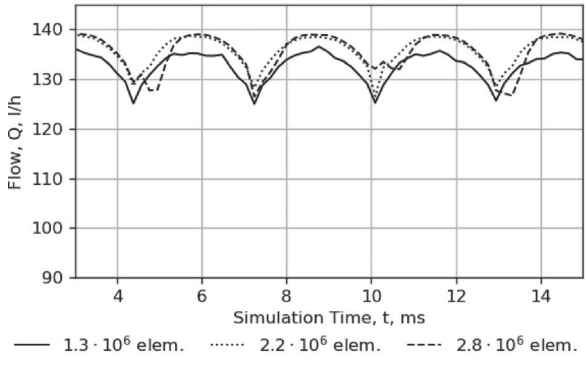

Figure 13. Volumetric efficiencies in relation to the simulation time step for three different mesh densities.

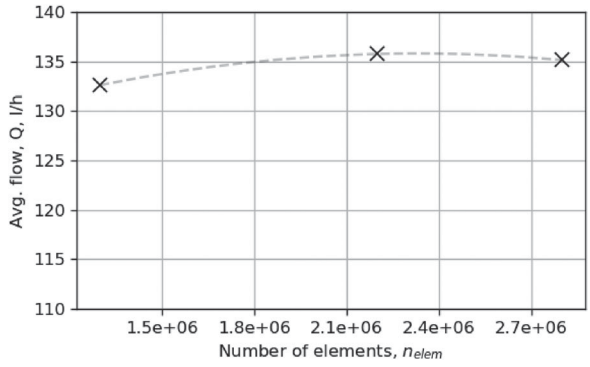

Figure 14. Relation between number of mesh elements and averaged volumetric efficiency.

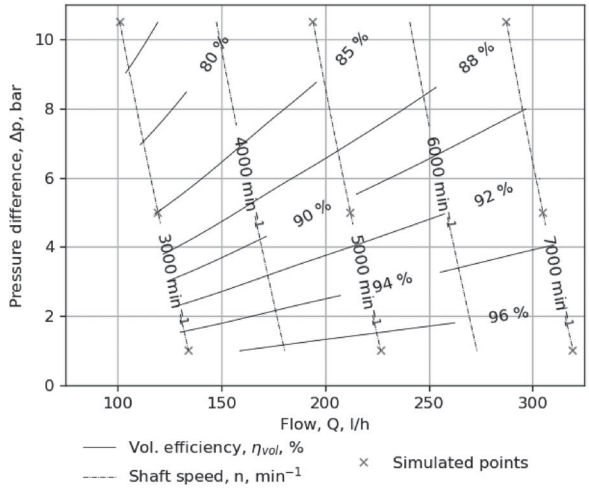

Figure 15. Numerically calculated contours of volumetric efficiencies and shaft rotation speeds in p-Q diagram.

4.2. Flow rate and volumetric efficiency

Volumetric flow rates and volumetric efficiencies were analyzed using full numerical model, which contains $4.9 \cdot 10^6$ elements. Performance maps in Figures 15 and 16 represent simulated and experimentally obtained volumetric efficiencies, respectively. Values between acquired operating points were obtained with cubic interpolation. On the performance map, which results from CFD analysis the contours of volumetric efficiency are almost linear, while the contours in Figure 16 have a non-linear shape. Simulated value of volumetric flow rate at 500 kPa and 5000 rpm is 212.3 l/h, while the measured value in the same operating point is 219.2 l/h.

Comparison of numerically and experimentally obtained flow rates, which are represented in Figures 15 and 16, shows that the results are comparable at the high-pressure region, while the deviations are the highest in the region of low pressure and low volumetric flow rate.

Differences can be attributed to two major reasons. First, in the case of experimental test pump parts are

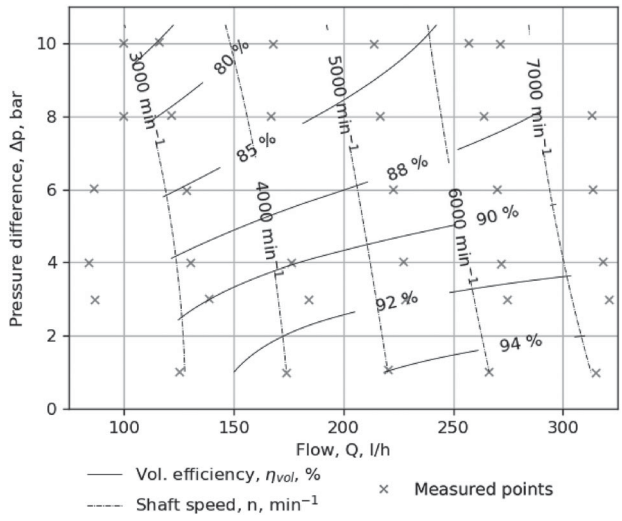

Figure 16. Experimentally obtained contours of volumetric efficiencies and shaft rotation speeds in p-Q diagram.

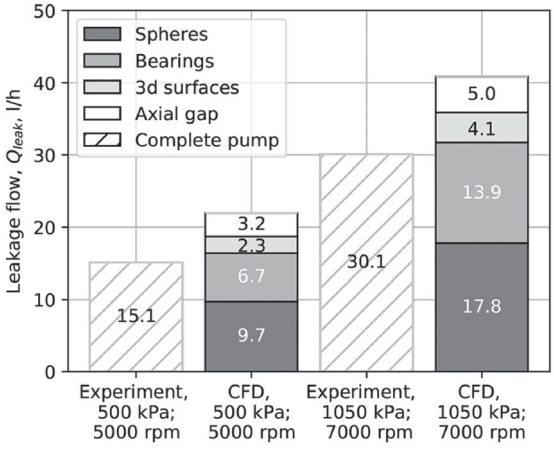

Figure 17. Contributions of different leakage paths in two operating points.

undergoing small axial motion, which can be correlated with geometry deviations or changes of the pressure field. Mentioned effects were not taken into the account in CFD analysis. Second, pressure can affect the positioning of the runner and the shaft and therefore cause a change of alignment of the parts, which also change the size of the gaps and finally effects internal leakage flows. Surface properties such as roughness and local geometrical deviations can also affect the reliability of the numerical model.

Detailed analysis of the flows inside of the pump shows that the leakage flow over the gaps between the spherical surfaces of pump parts has the most significant contribution to the overall leakage flow, following with the contribution of the leakage through journal bearing. Figure 17 shows separate contributions of leakage paths, which are labelled in Figure 4. Experimental leakage flows were calculated from the difference between the theoretical flow Q_{theor} and the measured flow Q_{meas} as follows:

$$Q_{leak} = Q_{theor} - Q_{meas} = q_{theor} \cdot n - Q_{meas}. \quad (3)$$

Simulated flows were extracted by isolating separate flow path contributions in the post-processing step.

4.2.1. Velocity and pressure fields

Absolute pressures in suction and delivery chambers are shown in Figure 18(a), while values on the pump runner and the shaft surfaces are presented in Figure 18(b).

Figure 18(b) gives a good overview of pressure distribution on the outer surfaces of the analyzed fluid region. The gradient between high and low-pressure chambers is clearly seen. It is also possible to notice the pressure gradient on the journal bearing.

Figures 19(a,b) show velocity and corresponding pressure fields, respectively. Peak velocity (see Figure 19a) occurs on the suction side of the pump in the vicinity of the pump runner surface. CFD results did not reveal the regions, where vapor pressure (3.17 kPa at the water temperature of 25°C) would occur. Nevertheless, by analyzing Figure 19(b), it is possible to notice that the absolute pressure value inside of the region (1) is near 10 kPa. Experimental results did not show performance

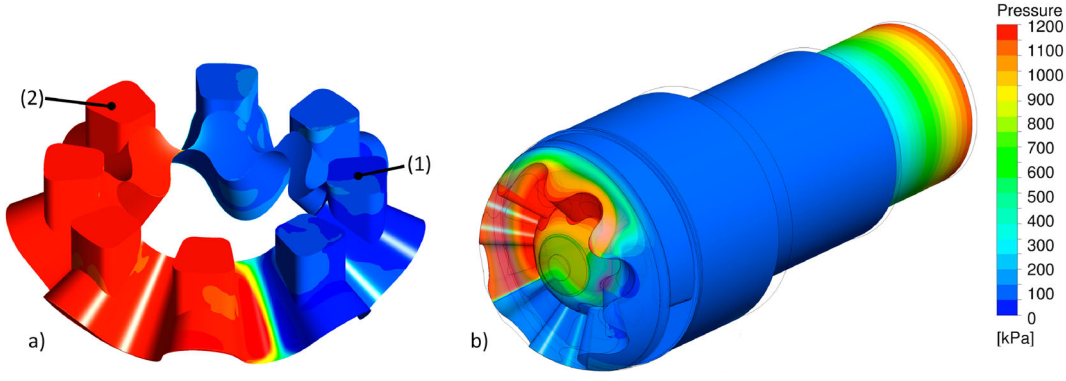

Figure 18. (a) Absolute pressure in suction (1) and delivery (2) chambers of the pump and (b) the pressure field on the pump stator and shaft surfaces.

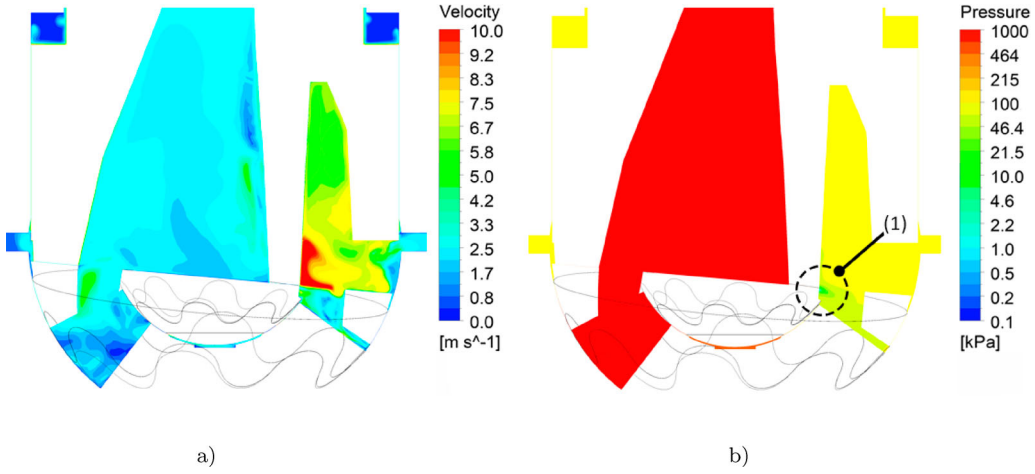

Figure 19. (a) Velocity field and (b) absolute pressure in the section of TMC pump.

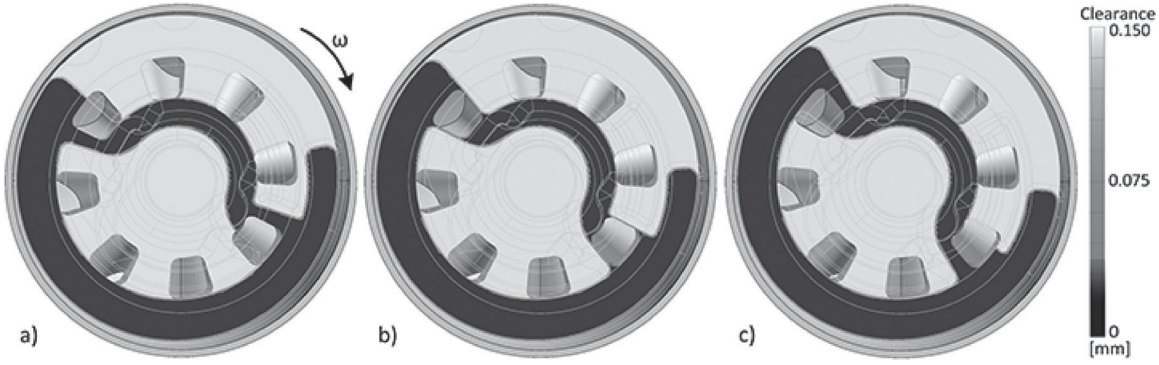

Figure 20. Sealing region between pump runner and the shaft for shaft rotations (a) $\theta = 19.1°$, (b) $\theta = 22.5°$, and (c) $\theta = 28.5°$.

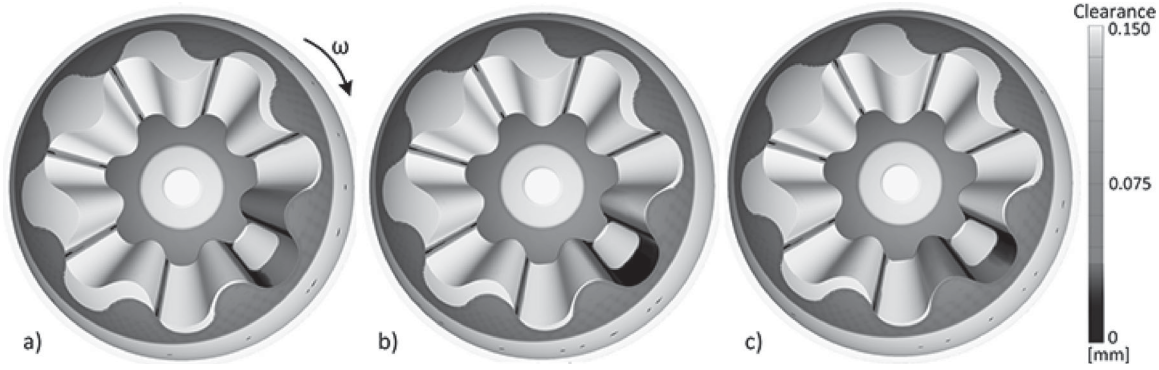

Figure 21. Sealing regions between pump stator and pump runner for shaft rotations (a) $\theta = 19.1°$, (b) $\theta = 22.5°$, and (c) $\theta = 28.5°$.

degradation related to the shaft speed (see Figure 16). The findings are valid for near-zero losses in the suction compartment of the hydraulic system, which was also the assumption in presented CFD study. However, the risk of cavitation increases with decreasing the inlet pressure, which could be investigated in a separate study.

Following results reveal more interesting findings. Figure 20 shows sealing regions in the vicinity of the valve plate, Figure 21 shows sealing lines between toothed parts and Figure 22 exposes corresponding pressure distributions for three time steps. Figures 20(a), 21(a) and 22(a) represent the state at shaft rotation $\theta = 19.1°$, which is just before the valve plate overlaps with the channel in the pump runner. From Figure 22(a), it is clear that the area (1) is still under low-pressure region and area (2) is located on the delivery side.

Shaft rotation $\theta = 22.5°$ is shown in Figures 20(b), 21(b) and 22(b). In this position, the surface of the valve plate completely covers the channel in pump runner. On the corresponding Figure 22(b), both regions (1) and (2)

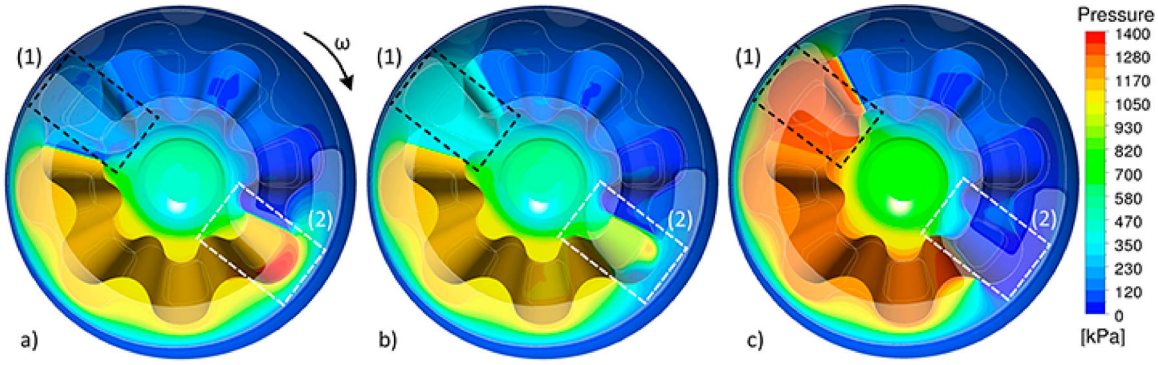

Figure 22. Pressure field on the stator for shaft rotations: (a) $\theta = 19.1°$, (b) $\theta = 22.5°$, and (c) $\theta = 28.5°$.

undergo the transition from the high or the low pressure regions to the region of average pressure.

Finally, Figures 20(c), 21(c) and 22(c) represent the rotation at $\theta = 28.5°$. On Figure 20(c), propagation of the sealing line can be seen. In comparison with the previous state (angle $\theta = 22.5°$), the edges on the shaft geometry at angle $\theta = 28.5°$ are not collinear with the contours on the pump runner, which means that the continuous sealing is established. Between Figures 21(b) and 21(c), there is no major change in the clearance between the pump stator and the runner.

From the pressure field in Figure 22(c), it is seen that the region (1) underwent to the delivery side of the pump and region (2) underwent to the suction side.

5. Conclusion

TMC pumps are generally unknown hydraulic devices, which have certain advantages over conventional PD pumps. Specific gear shapes and movement of the pump runner require unique approach to the design and analysis processes of TMC pumps. For this purpose, a method for simulating of pressure distribution and flow processes in TMC pump was developed. Results are presented together with the visualization of time-dependent spatial variations of the sealing regions between individual volumetric chambers and between low and high-pressure sides of the pump. After extensive study of the methods that allow modeling of deforming volumes in various PD pumps, we decided to use automatically generated meshes, exported from Twinmesh software.

The volumetric flow rate was taken under the investigation and the results yield that the most influential regions are the gaps between spherical surfaces and the regions between surfaces of journal bearings.

Results, obtained from numerical and experimental parts of the research, show similar trends in the majority of analyzed operating points. However, some limitations of conducted CFD analysis exist. The reasons for the deviations can be neglecting of axial movements, which are caused by small geometry deviations and the effects of the pressure balance in the pump. Pressure balance does, in fact, change positioning of the pump parts during the rotation of the pump shaft. Analysis of hydraulic and mechanical effects on the micro-motions as well as the influences on overall characteristics of the pump could be investigated in a separate research.

The analyzed system is characterized by the behavior affected by the transition phenomenon, which occurs when the valve plate moves relative to the channels in the runner. Varying the positions and the tightness of the sealing regions can affect pressure and flow ripple in the system. Pressure and flow ripples are known phenomena, which occur in many types of PD pumps. The ripples were investigated by Zhang et al. (2017) and Manring and Kasaragadda (2003). It is expected that similar effects could also be perceived in the case of TMC pump.

Besides the analysis of ripples, there are also a few other topics, which could be researched based on the developed procedure. Some options are featured below:

- Gap variations can affect the fluid flow and the forces working between the parts in PD pumps (Li et al., 2018). For TMC pump analysis, variations of the clearances in different sealing regions could be performed to optimize overall efficiency.
- Level of reliability of the numeric model could be confirmed with the study based on the statistical approach. Such an approach was demonstrated by Battarra and Mucchi (2020), who used LP model and experimental results for quantitative analysis of 20 nominally identical gear pumps.
- Specific flow conditions related to TMC principle can lead to cavitation on unknown locations. Future research could focus on the identification and analysis of critical regions on CFD and experimental basis.

Disclosure statement

No potential conflict of interest was reported by the author(s).

References

Altare G., & Rundo M. (2016). Computational fluid dynamics analysis of gerotor lubricating pumps at high-speed: Geometric features influencing the filling capability. *Journal of Fluids Engineering*, *138*(11), 111101. doi: https://doi.org/10.1115/1.4033675

Ansys cfx – solver theory guide: Release 14.0. (2011). Ansys, Inc.

Antoniak P., & Stryczek J. (2018). Visualization study of the flow processes and phenomena in the external gear pump. *Archives of Civil and Mechanical Engineering*, *18*, 1103–1115. doi: https://doi.org/10.1016/j.acme.2018.03.001

Arnold F. (1993). *Rotary-piston machine* (WO9312325A1). WIPO. https://patentscope.wipo.int/search/en/WO1993012325

Battarra M., & Mucchi E. (2020). On the assessment of lumped parameter models for gear pump performance prediction. *Simulation Modelling Practice and Theory*, *99*, 102008. doi: https://doi.org/10.1016/j.simpat.2019.102008

Battarra M., Mucchi E., & Dalpiaz G. (2015). A model for the estimation of pressure ripple in tandem gear pumps. *ASME IDETC/CIE*, Boston, USA 10. https://doi.org/10.1115/DETC2015-46338

Benek J., Steger J., Dougherty F., & Buning P. (1986). *Chimera. A grid-embedding technique*. NASA Ames Research Center.

Castilla R., Gamez-Montero P. J., Del Campo D., Raush G., Garcia-Vilchez M., & Codina E. (2015). Three-dimensional numerical simulation of an external gear pump with decompression slot and meshing contact point. *Journal of Fluids Engineering*, *137*(4), 041105. doi: https://doi.org/10.1115/1.4029223

Castilla R., Gamez-Montero P. J., Raush G., & Codina E. (2017). Method for fluid flow simulation of a gerotor pump using openFOAM. *Journal of Fluids Engineering*, *139*(11), 111101. doi: https://doi.org/10.1115/1.4037060

Chao Q., Zhang J., Xu B., Huang H., & Zhai J. (2019). Effects of inclined cylinder ports on gaseous cavitation of high-speed electro-hydrostatic actuator pumps: A numerical study. *Engineering Applications of Computational Fluid Mechanics*, *13*(1), 245–253. doi: https://doi.org/10.1080/19942060.2019.1576545

Chen T. T., Wang J. P., Huang G. M., Hsu M. H., Chen C. L., Hong B.-W., & Wey J.-M., 2018). High-precision technology with negative punch clearance for the manufacturing of a cycloid pump. *The International Journal of Advanced Manufacturing Technology*, *95*(1–4), 1179–1183. doi: https://doi.org/10.1007/s00170-017-1312-z

Frosina E., Senatore A., & Rigosi M. (2017). Study of a high-pressure external gear pump with a computational fluid dynamic modeling approach. *Energies*, *10*(8), 1113. doi: https://doi.org/10.3390/en10081113

Gamez-Montero P. J., Codina E., & Castilla R. (2019). A review of gerotor technology in hydraulic machines. *Energies*, *12*(12), 2423. doi: https://doi.org/10.3390/en12122423

Hsieh C. F. (2012). Fluid and dynamics analyses of a gerotor pump using various span angle designs. *Journal of Mechanical Design*, *134*(12), 121003. doi: https://doi.org/10.1115/1.4007703

Iannetti A., Stickland M. T., & Dempster W. M. (2016). A CFD and experimental study on cavitation in positive displacement pumps: Benefits and drawbacks of the 'full' cavitation model. *Engineering Applications of Computational Fluid Mechanics*, *10*(1), 57–71. doi: https://doi.org/10.1080/19942060.2015.1110535

Kim S. Y., Nam Y. J., & Park M. K. (2006). Design of port plate in gerotor pump for reduction of pressure pulsation. *Journal of Mechanical Science and Technology*, *20*(10), 1626–1637. doi: https://doi.org/10.1007/BF02916266

Kovacevic A., Stosic N., & Smith I. (2003, January). 3-D numerical analysis of screw compressor performance. *Journal of Computational Methods in Sciences and Engineering*, *3*. doi: https://doi.org/10.3233/JCM-2003-3206

Kunath S., Laforsch O., Kacmar M., Kling M., & Skrynski E. (2016). Förderaggregat DE 102014219219. DPMA.

Li Y. B., Guo D. S., & Li X. B. (2018). Mitigation of radial exciting force of rotary lobe pump by gradually varied gap. *Engineering Applications of Computational Fluid Mechanics*, *12*(1), 711–723. doi: https://doi.org/10.1080/19942060.2018.1517053

Liu Y. Y., An K., Liu H., Gong J. G., & Wang L. Q. (2019). Numerical and experimental studies on flow performances and hydraulic radial forces of an internal gear pump with a high pressure. *Engineering Applications of Computational Fluid Mechanics*, *13*(1), 1130–1143. doi: https://doi.org/10.1080/19942060.2019.1666746

Manring N. D., & Kasaragadda S. B. (2003). The theoretical flow ripple of an external gear pump. *Journal of Dynamic Systems, Measurement, and Control*, *125*(3), 396–404. doi: https://doi.org/10.1115/1.1592193

Menter F. (1993). Zonal two equation kw turbulence models for aerodynamic flows. *23rd fluid dynamics, plasmadynamics, and lasers conference 2906*. https://doi.org/10.2514/6.1993-2906

Menter F., Kuntz M., & Langtry R. (2003). Ten years of industrial experience with the SST turbulence model. *Turbulence, Heat and Mass Transfer*, *4*(1), 625–632.

Natchimuthu K., Sureshkumar J., & Ganesan V. (2010, April). CFD analysis of flow through a gerotor oil pump. *SAE technical papers*. https://doi.org/10.4271/2010-01-1111

Pellegri M., Vacca A., Devendran R., Dautry E., & Ginsberg B. (2016). A Lumped parameter approach for gerotor pumps: Model formulation and experimental validation. *Proceedings of the 10th international fluid power conference*, Dresden, Germany 8–10.

Prakash M., Stokes N., Bertolini J., Tatford O., & Gomme P. (2003). SPH simulations of a lobe pump: Prediction of protein shear stress at different pump efficiencies. *Proceedings of the 3rd international conference on CFD in minerals and process industries* (pp. 183–188). https://doi.org/10.1042/ba20050188

Rhie C., & Chow W. L. (1983). Numerical study of the turbulent flow past an airfoil with trailing edge separation. *AIAA Journal*, *21*(11), 1525–1532. doi: https://doi.org/10.2514/3.8284

Robison A., & Vacca A. (2018). Multi-objective optimization of circular-toothed gerotors for kinematics and wear by genetic algorithm. *Mechanism and Machine Theory*, *128*, 150–168. doi: https://doi.org/10.1016/j.mechmachtheory.2018.05.011

Rundo M. (2017, August). Models for flow rate simulation in gear pumps: A review. *Energies*, *10*, 1261. doi: https://doi.org/10.3390/en10091261

Spille-Kohoff A., & Hesse J. (2016, September). CFD simulation of cavitation in an internal gear pump. *35. CADFEM ANSYS simulation conference*.

Spille-Kohoff A., Hesse J., & Andres R. (2017). Grid generation and CFD simulation for positive displacement machines. *NAFEMS World congress*.

Steger J. L., Dougherty F. C., & Benek J. A. (1983). *A chimera grid scheme* (Vol. 5). American Society of Mechanical Engineers.

Strmčnik E., Majdič F., & Kalin M. (2019, March). Water-lubricated behaviour of AISI 440C stainless steel and a DLC coating for an orbital hydraulic motor application. *Tribology International*, *131*, 128–136. doi: https://doi.org/10.1016/j.triboint.2018.10.032

Voorde J. V., Vierendeels J., & Dick E. (2004). Development of a Laplacian-based mesh generator for ALE calculations in rotary volumetric pumps and compressors. *Computer Methods in Applied Mechanics and Engineering*, *193*(39–41), 4401–4415. doi: https://doi.org/10.1016/j.cma.2003.12.063

Wildhaber E. (1966). *Positive-displacement unit* (US3236186A). United States Patent Office. https://patents.google.com/patent/US3236186A

Wildhaber E. (1974). *Rotor pair for positive fluid displacement* (US3856440A). United States Patent Office. https://patents.google.com/patent/US3856440A.

Yoon Y., Park B., Shim J., Han Y. O., Hong B. J., & Yun S. H. (2017, March). Numerical simulation of three-dimensional external gear pump using immersed solid method. *Applied Thermal Engineering*, *118*. doi: https://doi.org/10.1016/j.applthermaleng.2017.03.014

Zhang B., Ma J., Hong H., Yang H., & Fang Y. (2017). Analysis of the flow dynamics characteristics of an axial piston pump based on the computational fluid dynamics method. *Engineering Applications of Computational Fluid Mechanics*, *11*(1), 86–95. doi: https://doi.org/10.1080/19942060.2015.1091686

Zhang D., Perng C., & Laverty M. (2006). Gerotor oil pump performance and flow/pressure ripple study. *SAE 2006 World congress & exhibition*.

Zhao X., Vacca A., & Dhar S. (2018). Numerical modeling of a helical external gear pump with continuous-contact gear profile: A comparison between a lumped-parameter and a 3D CFD approach of simulation. *BATH/ASME 2018 symposium on fluid power and motion control*. https://doi.org/10.1115/FPMC2018-8903

Ziviani D., Suman A., Gabrielloni J., Pinelli M., De Paepe M., & M. van den Broek (2016). *CFD approaches applied to a single-screw expander*.